Broadband and Output-Controllable Triboelectric Nanogenerator Enabled by Coupling Swing-Rotation Switching Mechanism with Potential Energy Storage/Release Strategy for Low-Frequency Mechanical Energy Harvesting

Bao Cao, Peihong Wang,* Pinshu Rui, Xiaoxiang Wei, Zixun Wang, Yaowen Yang, Xinbo Tu, Chen Chen, Zhongzhu Wang, Zhuoqing Yang, Tao Jiang, Jia Cheng,* and Zhong Lin Wang*

Irregular and low-frequency mechanical energy, including ocean energy, is widely distributed but mostly wasted. Triboelectric nanogenerator (TENG) has been proved as a very promising ocean energy harvesting technology. However, the traditional cylindrical pendulum TENG (CP-TENG) can only work effectively in a narrow frequency bandwidth. In this work, a triboelectric nanogenerator enabled by coupling the swing-rotation switching mechanism with a potential energy storage/release strategy (SR-TENG) is presented. It can convert various swing/vibration mechanical energies into electric energy, and it has a controllable output performance whether it works under intermittent rotation mode or continuous rotation mode. This coupling results enable SR-TENG to efficiently harvest low-frequency mechanical energy from 0.3 to 5 Hz. Therefore, its bandwidth is about four times larger than that of CP-TENG. The peak power density of SR-TENG can reach 10.1 W m^{-3} at 1.8 Hz and 15.4 W m^{-3} at 5 Hz, respectively. Moreover, its durability is improved greatly due to its non-contact working mode. Based on this SR-TENG, several applications toward smart ocean, including a self-powered and wireless hydrological information monitoring system, are demonstrated successfully. These strategies are very helpful to improve the bandwidth, the output performance, and the durability of TENGs.

1. Introduction

With the rapid development of the world economy, energy has always been the focus of social attention. The widespread use of traditional fossil energy has gradually caused new energy crises and environmental problems.[1] Therefore, it is very necessary to explore new energy sources.[2] Meanwhile, with the development of wireless sensor networks and the Internet of Things,[3] traditional power supply technology not only requires tedious manual operations such as replacement, charging, and maintenance, but also causes bad effects on the environment.[4] There is an urgent need for a sustainable, distributed, self-powered, and environmentally friendly power source to power distributed sensors. The triboelectric nanogenerator (TENG) proposed by Prof. Z. L. Wang in 2012 is based on the coupling effect of electrostatic induction and triboelectric electrification.[5] Due to its small size, low

B. Cao, P. Wang, P. Rui, X. Wei, Z. Wang, Y. Yang, X. Tu,
C. Chen, Z. Wang
School of Materials Science and Engineering
Energy Materials and Devices Key Lab of Anhui Province
for Photoelectric Conversion
Anhui University
Hefei, Anhui 230601, China
E-mail: wangpeihong2002@ahu.edu.cn
P. Wang
Key Laboratory of Structure and Functional Regulation
of Hybrid Materials
Anhui University
Ministry of Education
Hefei, Anhui 230601, China

The ORCID identification number(s) for the author(s) of this article can be found under https://doi.org/10.1002/aenm.202202627.

DOI: 10.1002/aenm.202202627

Z. Yang
School of Electronic Information and Electrical Engineering
Shanghai Jiao Tong University
Shanghai 200240, China
T. Jiang, Z. L. Wang
Beijing Institute of Nanoenergy and Nanosystems
Chinese Academy of Sciences
Beijing 101400, China
J. Cheng
State Key Laboratory of Tribology
Department of Mechanical Engineering
Tsinghua University
Beijing 100084, China
E-mail: chengjia@tsinghua.edu.cn
Z. L. Wang
School of Materials Science and Engineering
Georgia Institute of Technology
Atlanta, GA 30332, USA
E-mail: zhong.wang@mse.gatech.edu

cost, simple operation, and high energy conversion efficiency,[6] TENG has gradually shown excellent application potential in harvesting various mechanical energy.[7] Compared with electromagnetic generator (EMG), TENG does not rely on bulky magnetic components, and has higher energy harvesting efficiency than EMG at low frequency.[8] Therefore, TENG has received more and more attention from researchers in recent years.

In order to harvest ambient low-frequency mechanical energy, many cylindrical pendulum TENGs (CP-TENGs) are proposed and studied systematically by lots of researchers. However, they has some same problems, such as low average power density and narrow working frequency band.[9] Only when the excitation frequency is close to the natural frequency of the CP-TENG device, does it have good output performance; if the excitation frequency deviates from the natural frequency, CP-TENG hardly works, and the stability of its output energy and energy conversion efficiency is extremely low. For example, the CP-TENG designed by our group [10] reduced the running resistance of the rotor due to the introduction of the arched film structure, but it hardly works under extremely low frequency (d1 Hz), and the output performance drops sharply if excitation frequency deviates from the optimal working frequency. On the other hand, the rotary TENG has the advantages of high output power density and dense output current signal,[11] but it has the defect of not being able to directly collect swing and linear energy, which limits the application range of the rotary TENG. It is necessary to design a novel energy switching structure, which can convert linear mechanical energy into rotational energy and reform the application defects of the traditional CP-TENG. In addition, due to the lack of structural design of TENG, irregular external trigger results in random output performance of the TENG device.[12] Some mechanical adjustment methods are required to obtain controllable electrical energy. A mechanical regulation triboelectric nanogenerator (MR-TENG) designed by Yin et al. [13] mainly relies on compression springs to achieve energy storage and realize controllable electrical energy. Due to the friction resistance of the complicated mechanical structure, MR-TENG does not respond well to very low frequencies. Besides, MR-TENG always needs multiple excitations to store energy and has no output in the energy storage stage. In order to make up for these deficiencies, and the working frequency band need to be further broadened, it is necessary to design a new structure of TENG with lower friction resistance to improve application prospect.

Herein, a triboelectric nanogenerator enabled by the swing-rotation switching mechanism (SR-TENG) is presented to harvest mechanical vibration and water wave energy. The introduction of the swing-rotation switching mechanism enables the SR-TENG to convert external linear and swing energy into rotational energy and then convert it into output-controllable electric energy. With the excitation energy increasing, SR-TENG, based on the proposed potential energy storage/release strategy, can automatically switch between intermittent rotation mode and continuous rotation mode. Due to the unique mechanism and low friction resistance, SR-TENG can harvest low-frequency mechanical energy from 0.3 to 5 Hz. Based on theoretical analysis, the influence of the natural frequency of the swinging component and the excitation energy on the energy switching structure was explored first, and

then the mechanical behaviors and output characteristics of SR-TENG under various mechanical triggering conditions were systematically revealed. After that, SR-TENG was demonstrated to successfully drive several electronic devices and light up 1620 LEDs. Finally, toward smart ocean, we successfully performed the demonstrations on marine lighting and rescue, the expulsion of microorganisms, ambient temperature and humidity detection. This work provides an idea for researchers trying to expand the application range of TENG through a simple and effective mechanical adjustment.

2. Results and Discussion

2.1. Structure and Working Principle of SR-TENG

Figure 1a shows the potential application of the SR-TENG network working on the ocean. SR-TENGs can be made into buoys to collect water wave energy, which is committed to self-powered wireless transmission of various marine affairs and of information. The schematic diagram of SR-TENG is illustrated in Figure 1b. SR-TENG mainly includes three parts, an internal rotor, an external stator and a swing-rotation switching structure (SRSS). The rotor consists of an acrylic cylinder and mass block II. On its outer wall, 16 fluorinated ethylene propylene (FEP) films and Nylon films are spaced in sequence. The inner wall of the acrylic stator adheres with 28 copper (Cu) electrodes. In order to improve the response of the device to the external extremely low-frequency excitation, there is a gap (about 1.3 mm) between the rotor and the stator, which greatly reduces resistance and improves the durability of the device. Meanwhile, two blade-type FEP films are respectively pasted on the inner wall of the stator at symmetrical positions. One blade-type FEP film occupies the position of two Cu electrodes and therefore the number of Cu electrodes is 28. The blade-type FEP films are used as the charge pump [14] to continuously provide charges to the film on the rotor. In this way, the charge dissipation problem of non-contact TENG is better solved. Figure S1a,b, Supporting Information shows the physical map of the electrode layer, the charge pump, and two dielectric films. As shown in Figure S1c, Supporting Information, the SRSS consists of a fan-shaped swinging component with the central angle of 60° supported by the one-way clutch II through the center shaft, and the mass block I is added to the bottom of the swinging component to lower the center of gravity. The inner rings of two one-way clutches and bearing are fixed together with the central shaft, and the central shaft is fixed with the rotor. The installation direction of the two one-way clutches is the same, that is, the center shaft can only rotate in one direction and lock in the opposite direction. So, the swinging component can control the one-way clutch II to realize the unidirectional rotation of the rotor. Finally, the electricity is generated by SR-TENG. It is worth mentioning that the unidirectional rotation direction of the rotor can be controlled by adjusting the installation method of the clutches. Meanwhile, all clutch connections are treated with lubricating oil, which further reduces frictional resistance. More experimental details can be seen in the Experimental Section.
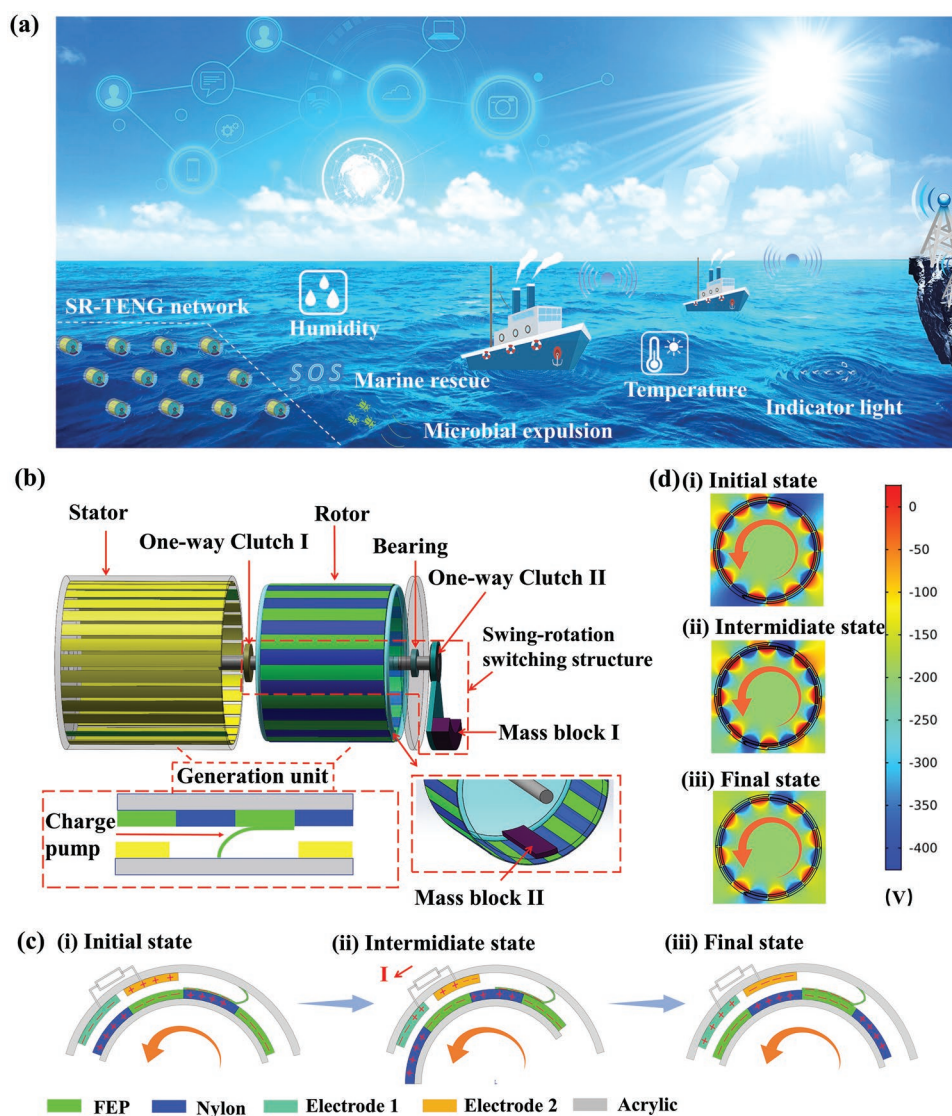
**ADVANCED
SCIENCE NEWS**
www.advancedsciencenews.com

**ADVANCED
ENERGY
MATERIALS**
www.advenergymat.de

Figure 1. The triboelectric nanogenerator is enabled by the swing-rotation switching structure (SR-TENG). a) Schematic diagram of the SR-TENG network for harvesting wave energy. b) The detailed structure of the SR-TENG. c) The working principle and d) the simulation in different working states of SR-TENG.

Figure 1c shows the working principle of SR-TENG under external triggering. With the unidirectional rotation of the rotor, the blade-type FEP film of the stator contacts the Nylon film of the rotor, positive charges are generated on the surface of the Nylon film, and negative charges are generated on the surface of the blade-type FEP film. After continuously cyclic contact, the triboelectric charges get saturated. As shown in Figure 1c-i, the Nylon film and the FEP film of the rotor completely face electrode 1 and electrode 2, respectively. In the initial state, the corresponding opposite charges are induced on electrode 1 and electrode 2. When an external trigger causes the rotor to rotate counterclockwise, the Nylon and FEP film partly face electrode 1 and electrode 2. The electrons in electrode 1 flow into electrode 2, generating current in the external circuit, as shown in Figure 1c-ii. As demonstrated in Figure 1c-iii, the current continues until the Nylon and FEP film completely face electrode 2 and electrode 1, respectively. Here we only introduce the first

half of the current generation process, the working principle of the reverse current is very similar. To verify the feasibility of the power generation principle, the COMSOL Multiphysics software was used to perform the theoretical analysis of these states by using the finite element method (Figure 1d). As the relative position between the rotor and the stator changes, the simulated potential profile shows the potential difference between the two electrodes generating the alternating current in the external circuit. The periodic oscillation of the swinging component under external triggering drives the rotor to rotate unidirectionally, thereby the TENG generates periodic alternating electrical output signals.

According to the level of the external excitation energy, SR-TENG has two working modes of intermittent and continuous rotation. **Figure 2**a shows the specific process in the intermittent rotation mode. As shown in Figure S2, Supporting Information, the angle between the straight line formed by the

**ADVANCED
SCIENCE NEWS**

www.advancedsciencenews.com
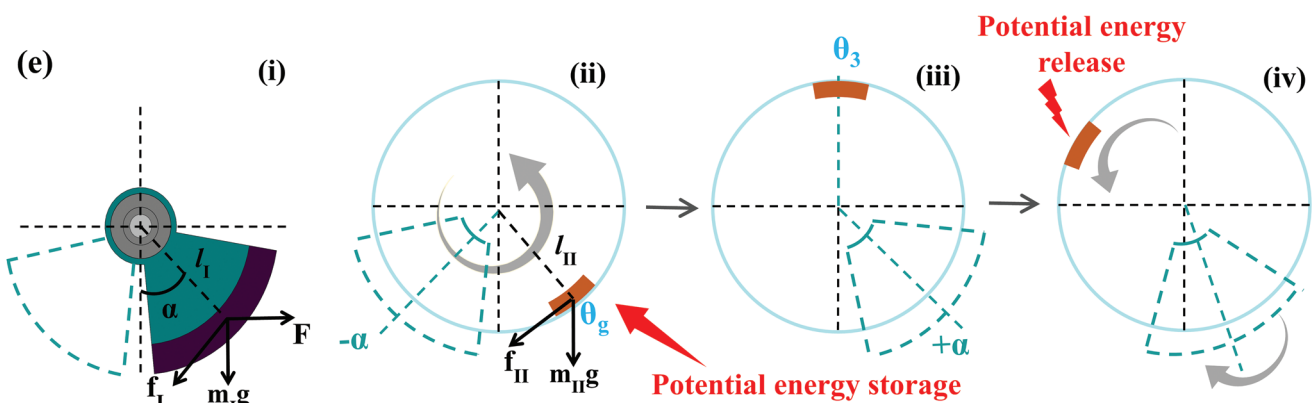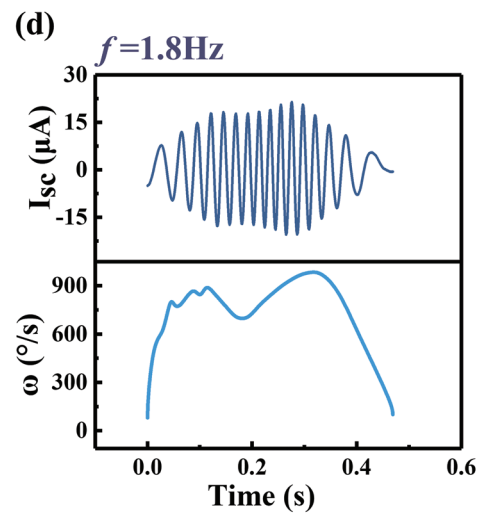
**ADVANCED
ENERGY
MATERIALS**
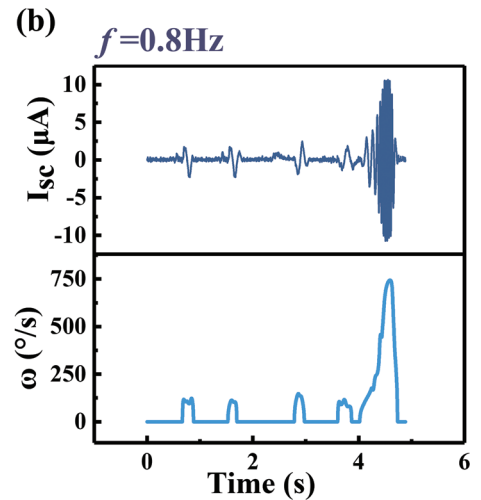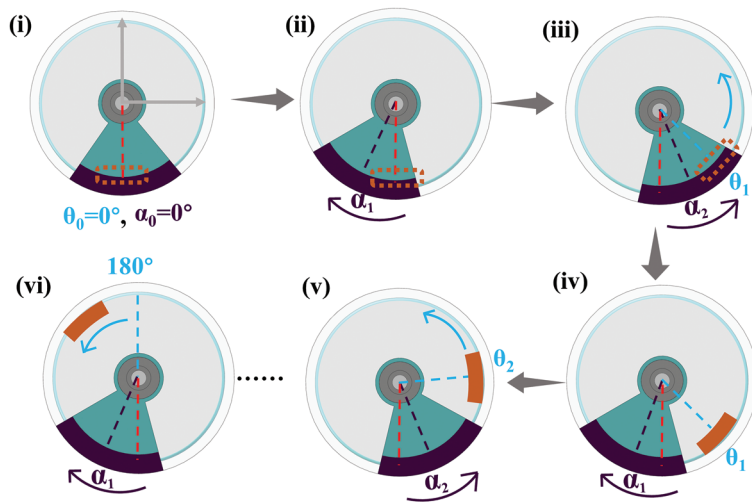
www.advenergymat.de
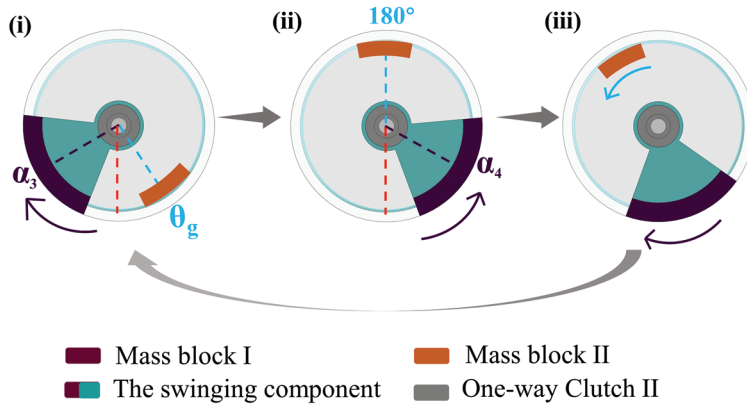
Figure 2. The operating process and typical performance of the SR-TENG. Schematic diagram of SR-TENG driven by external trigger and the I_{sc} and ω versus time of a,b) intermittent rotation mode and c,d) continuous rotation mode. e) The theoretical model of SR-TENG.

shaft center and the mass center of mass block II and the vertical line through shaft center is defined as θ, and the angle between the straight line formed by the shaft center and the mass center of mass block I and the vertical line through shaft center is defined as α. Meanwhile, the counterclockwise direction is

set as the positive direction. In the initial state as shown in Figure 2a-i, both of the two mass blocks are at the bottom ($\theta_0 = 0°$, $\alpha_0 = 0°$). As shown in Figure 2a-ii, the swinging component turns clockwise to α_1 and the rotor is stationary when SR-TENG is driven by external small energy. When the

**ADVANCED
SCIENCE NEWS**

www.advancedsciencenews.com

**ADVANCED
ENERGY
MATERIALS**

www.advenergymat.de

swinging component turns counterclockwise from α_1 to α_2, the outer ring of the one-way clutch II cannot rotate freely in the counterclockwise direction, so the rotor rotates counterclockwise to θ_1, as demonstrated in Figure 2a-iii. As shown in Figure 2a-iv, when the swinging component turns clockwise again, the rotor remains unchanged at θ_1 due to the joint action of two one-way clutches. Figure 2a-v shows the swinging component turns counterclockwise from α_1 to α_2 again, the rotor rotates to θ_2. After several external triggers, when the mass block II rises to the highest point ($\theta = 180°$), the rotor rotates counterclockwise without external excitation due to the gravitational potential energy release of the mass block II, as shown in Figure 2a-vi. As shown in Figure 2a, the rotor can only rotate one cycle after several stops, so this process is defined as intermittent rotation mode.

Figure 2b shows the short-circuit current (I_{sc}) of SR-TENG in intermittent rotation mode and the angular velocity (ω) of the rotor at $f = 0.8$ Hz. The angular velocity was obtained by using the formula $\omega = \dfrac{d\theta}{dt}$ based on the curve of the angle (θ) of the rotor shown in Figure S3, Supporting Information. As can be seen in Figure 2b, $\omega = 0$ means the rotor remains stationary, so no current is generated, and the small current can be generated every time the rotor rotates at a small angular velocity. Finally, the rotor releases the stored gravitational potential energy and the SR-TENG generates a large current.

Figure 2c shows the specific process in the continuous rotation mode. In the following analysis, we assume that mass block II can reach the position of θ_g after it totally releases its gravitational potential energy every time. As shown in Figure 2c(i,ii), the swinging component turns counterclockwise from α_3 to α_4 when SR-TENG is driven by external large energy. Under the action of mass block I, mass block II can rotate from θ_g to $180°$ (or $>180°$) through a single trigger. Then mass block II can release its gravitational potential energy automatically and so the rotor continues to rotate downward, as shown in Figure 2c-iii. Meanwhile, mass block I starts rotating clockwise until the swing-rotation switching structure returns to the condition of Figure 2c-i. During the process that mass block II returns to the position of θ_g after passing the highest point ($\theta = 180°$) from the position of θ_g, mass block II is always rotating and has no stop. Therefore, this process is defined as continuous rotation mode.

Figure 2d shows the I_{sc} and ω versus time at $f = 1.8$ Hz when SR-TENG is under continuous rotation mode. It is clear that the angular velocity is always larger than zero and so the rotor keeps rotating. Moreover, the angular velocity value is much larger than that in intermittent rotation mode as shown in Figure 2b. Therefore, SR-TENG generates continuous current output and the I_{sc} value is also very large as shown in Figure 2d. In order to understand the working principle more easily, the structure explosion diagram and the switching process of the two modes of SR-TENG are simulated and the results are shown in Video S1, Supporting Information.

In order to further demonstrate the dynamic properties of the SR-TENG, a simplified model is proposed as shown in Figure 2e. Here the swinging component is regarded as a large-angle compound pendulum motion (Figure 2e-i). The inertial force and acceleration applied to the swinging component can be expressed as:

$$F = m_1 a \tag{1}$$

$$a = \left(2\pi f^2\right) A \cos\left(2\pi ft\right) \tag{2}$$

where m_1, f, A, and t are the quality of mass block I, excitation frequency, excitation amplitude, and time of the forced vibration. Based on force analysis, the moment balance equation of the swinging component is as follows:

$$J_I \frac{d^2\alpha}{d^2t} = -m_1 g l_1 \sin\alpha + \left(2\pi f^2\right) m_1 A \cos\left(2\pi ft\right) l_1 \cos\alpha + M_{f_1} \tag{3}$$

where J_I and α are the rotational inertia and the angular displacement of the swinging component, respectively. l_I is the distance from the central axis to the center of the mass block I, g is the gravitational acceleration, f_I is the friction force on the swinging component, and M_{fl} is the moment of f_I. According to Equation (3), we can get the value of α of the swinging component under certain external excitation conditions.

As shown in Figure 2e-ii, the swing component and the mass block II turn counterclockwise under external excitation. The position of the swinging component changes from $-\alpha$ to $+\alpha$ and the mass block II rotates from θ_g to θ_3, as indicated in Figure 2e-iii. Accordingly, mass block II converts obtained kinetic energy into its gravitational potential energy. This is the potential energy storage process. Here, the energy that the swinging component obtained from external excitation can be described as follows:

$$W_{1F} = \int_{-\alpha}^{+\alpha} F l_1 \cos\alpha \, d\alpha = \int_{-\alpha}^{+\alpha} \left(2\pi f^2\right) m_1 A \cos\left(2\pi ft\right) l_1 \cos\alpha \, d\alpha \tag{4}$$

According to the work-energy principle, the following equation can be obtained:

$$\begin{aligned} W_{1F} &= W_{1f} + W_{2f} + \Delta E_{p2} = W_{1f} + W_{2f} + m_{II} g l_{II} \left(\cos\theta_g - \cos\theta_3\right) \\ &= W_{1f} + W_{2t} \end{aligned} \tag{5}$$

where W_{1f} is the energy loss of the swinging component due to friction force, W_{2f} is the energy loss of mass block II due to friction force, ΔE_{p2} is the difference of potential energy of mass block II, l_{II} is the distance from the central axis to the center of mass block II, and W_{2t} is the total energy that mass block II obtained from outside.

The minimum value of the energy that drives mass block II to rotate from θ_g to $180°$ in one triggering can be described as follows:

$$W_{2t,threshold} = W_{2f} + m_{II} g l_{II} \left(1 + \cos\theta_g\right) \tag{6}$$

If $\theta_3 < 180°$, mass block II cannot rotate to its highest position in one triggering. This means that its obtained energy is not sufficient to make it go pass the highest point of its potential energy, namely $W_{2t} < W_{2t,\,threshold}$. At this time, SR-TENG works in intermittent rotation mode.

If $\theta_3 \geq 180°$, as shown in Figure 2e-iv, mass block II can rotate continuously due to the potential energy release, which

**ADVANCED
SCIENCE NEWS**

www.advancedsciencenews.com

**ADVANCED
ENERGY
MATERIALS**

www.advenergymat.de

means that $W_{2t} \geq W_{2t, threshold}$. Under this condition, SR-TENG works in continuous rotation mode.

According to the forced vibration mechanism, it can be seen from Equations (1), (2), and (4) that W_{1F} is proportional to the square of the external excitation frequency (f^2) and excitation amplitude (A). In subsequent experiments, we mainly adjust the value of A and f of the linear motor to control the value of W_{1F} ($A = \dfrac{a}{32f^2}$), and then study the characteristics of SR-TENG in two working modes.

Compared to traditional CP-TENG, we explain the novel advantages of SR-TENG from the perspective of the resonance frequency. Here the natural frequency of the swinging component is defined as f_s, which can be calculated according to the following formula:

$$f_s = \frac{1}{2\pi \sqrt{\dfrac{J_I}{m_I g l_I}}} \qquad (7)$$

if $f \approx f_s$, CP-TENG can realize good output performance. SR-TENG also works in continuous rotation mode due to the large angular displacement of the swinging component, and the output performance is also good. Subsequent experimental data also proved this. If $f \ll f_s$ and $f \gg f_s$, SR-TENG can still work in the intermittent rotation mode and continuous rotation mode, respectively. On the contrary, CP-TENG hardly works and so its output is extremely low when $f \ll f_s$ and $f \gg f_s$. Therefore, SR-TENG has broader bandwidth than CP-TENG.

2.2. Study on the Swing-rotation Switching Mechanism

The swing-rotation switching mechanism of SR-TENG is studied first, since it is very helpful for understanding the motion behavior and subsequent performance optimization of the SR-TENG. The schematic diagram of the experimental test is shown in **Figure 3**a. A linear motor is used to supply external excitation for the SR-TENG and an angle sensor is used to monitor the real-time rotation angle of the rotor. In the experiment, the excitation acceleration (a) is set as 3 m s^{-2} and the excitation amplitude (A) is changed. Meanwhile, the mass of mass block II is fixed as 50 g and the mass ratio of mass block I and II (defined as $i = m_I:m_{II}$) is changed. The value of i is adjusted from 4:1 ($m_I = 200$ g) to 6:1 ($m_I = 300$ g). In the following discussion, SRSS ($i = 4$) is defined as the swing-rotation switching structure with $i = 4:1$, SRSS ($i = 5$) and SRSS ($i = 6$) are also defined in this way.

Figure 3b shows the dependence of the rotation angle of the rotor with SRSS ($i = 5$) on the time under various amplitudes. When A is 10, 40, and 50 mm, each curve has several plateaus. The plateau means that the angle of the rotor is fixed and so the rotor is stationary at this time. Therefore, the SR-TENG works in intermittent rotation mode when A is 10, 40, and 50 mm. However, the SR-TENG works in continuous rotation mode when A is 20 mm and 30 mm, because the angle of the rotor is continuously changing. As shown in Figure 3b, the intermittent energy storage time of the rotor is defined as t_1, the energy release time is defined as t_2, and the period is defined

as $T = t_1 + t_2$. The rotation angle of the rotor versus the time for SRSS ($i = 4$) and SRSS ($i = 6$) are given in Figure S4, Supporting Information. SRSS ($i = 4$) also has the similar trend with SRSS ($i = 5$) as A increases, except that the continuous rotation mode appears when A is 30 and 40 mm. However, SRSS ($i = 6$) always exhibits intermittent rotation behavior. This shows that the amplitude region corresponding to the two modes changes significantly with changing i. As shown in Figure 3c, the value of T is obtained from Figure 3b and Figure S4, Supporting Information, which intuitively reveals the above phenomenon. For SRSS ($i = 5$), the value of T is relatively smaller than SRSS ($i = 4$) and SRSS ($i = 6$) at most amplitudes. It is apparent that different values of i directly affect the characteristics of the energy switching mechanism, so the response mode of SR-TENG to external excitation is also different. In the intermittent rotation mode (Figure 3d–f), due to the non-contact characteristics and the simple structure, SRSS can respond effectively to extremely low frequency (≤ 1 Hz). Here, the excitation parameter is A = 70 mm. Figure 3d shows the θ versus time curve of SRSS ($i = 5$) at different frequencies. When $f = 0.7$ Hz, after SRSS ($i = 5$) rotates intermittently for 9 s ($t_1 = 9$ s), it starts to release the stored gravitational potential energy. As f increases, the value of t_1 decreases. Figure S5, Supporting Information, is the data supplement of SRSS ($i = 4$) and SRSS ($i = 6$) for this excitation condition. As shown in Figure 3e, when f increases from 0.6 to 1 Hz, the value of t_1 of SRSS ($i = 4$) is larger than SRSS ($i = 5$) and SRSS ($i = 6$). The values of t_1 of SRSS ($i = 5$) and SRSS ($i = 6$) are both relatively smaller and similar. This shows that increasing i is beneficial to improving the response of SR-TENG to extremely low frequency. But if the value of i is too higher, there is no obvious better effect, which may depend on the appropriate matching mechanism. In addition, as shown in Figure 3f, we further study the dependence of energy release time on the excitation frequency with various i. The value of t_2 is between 0.7 and 0.8 s in the frequency band of 0.6–0.8 Hz, the reason is that the initial position of releasing the gravitational potential energy is similar, and the gravitational potential energy changes little. It is worth mentioning that the value of t_2 is between 0.6 and 0.7 s in the frequency band of 0.9–1 Hz. There is rotational kinetic energy in the initial position of the energy release stage provided by external excitation.

Then, in the continuous rotation mode, the excitation parameter is A = 20 mm. Figure 3g is the rotor rotation angle curve of SRSS ($i = 5$) when f changes. The experimental results show that it can realize continuous rotation in a wide frequency band. As f increases, the value of T decreases. Figure S6, Supporting Information, shows the corresponding data for SRSS ($i = 4$) and SRSS ($i = 6$) that exhibit similar continuous rotation trend. As shown in Figure 3h, the value of T and average angular velocity of the three are almost same, which shows that the value of i has little effect on the continuous rotation mode of SR-TENG.

Based on the above structural optimization and analysis, SRSS ($i = 5$) takes less time to rotate in the intermittent rotation mode, and it exhibits great mechanical characteristics that automatically switching to the continuous rotation mode without human intervention, and the continuous rotation mode of SRSS ($i = 5$) can be realized in a wide frequency band. Therefore, the SRSS ($i = 5$) is selected as the experimental parameter of TENG for subsequent experiments.
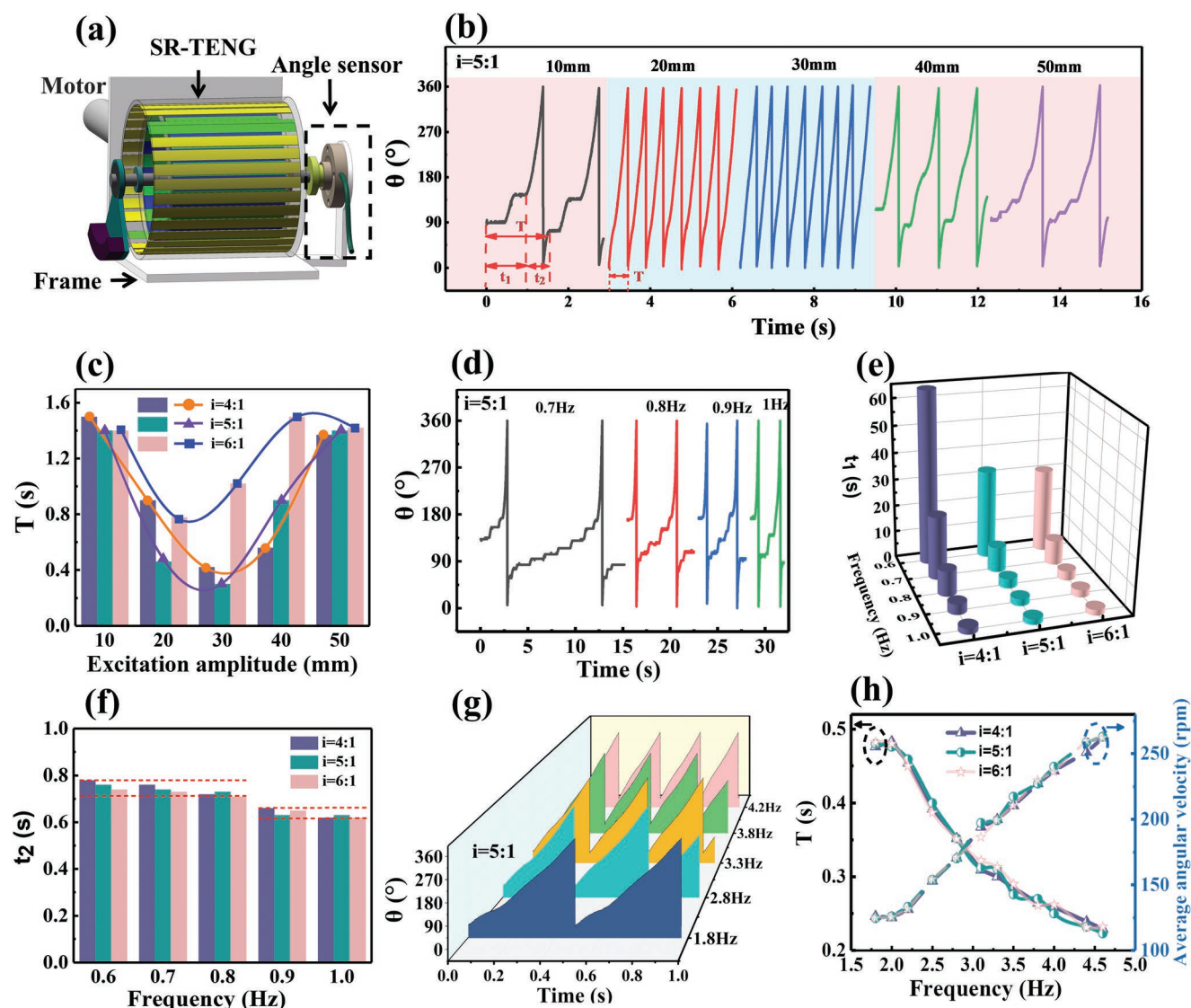
**ADVANCED
SCIENCE NEWS**

www.advancedsciencenews.com

**ADVANCED
ENERGY
MATERIALS**

www.advenergymat.de

Figure 3. Study on the swing-rotation switching mechanism of the SR-TENG under different conditions driven by the motor. a) The schematic diagram of monitoring the rotor rotation angle. b) Dependence of the rotor rotation angle of SRSS ($i = 5$) on the time with various amplitudes. c) The relationship between period and amplitude with different values of i. d) The relationship between rotor rotation angle and time at different extremely low frequencies for SRSS ($i = 5$) in intermittent rotation mode. Dependence of e) the intermittent energy storage time and f) energy release time on the frequency with various i. g) Dependence of the rotor rotation angle on the time under various frequencies for SRSS ($i = 5$) in continuous rotation mode. h) Dependence of the period and average angular velocity on the frequency with various i.

2.3. Output Performance of SR-TENG under Intermittent Rotation Mode

The electrical performance of SR-TENG under intermittent rotation mode is measured and analyzed in detail in this part. The short-circuit current of SR-TENG under different f and fixed excitation amplitude ($A = 70$ mm) are given in **Figure 4**a ($f = \approx 0.7$–1.0 Hz) and Figure S7, Supporting Information ($f = \approx 0.3$–0.6 Hz). It is clear that these current curves are similar. Every curve includes some small current peaks (<4 μA) and one large current peak (>10 μA). From the dynamic analysis of SRSS above, we know that the region including many small current peaks corresponds to the gravitational potential energy storage progress. Similarly, the appearance of the large current

peak means the release of the gravitational potential energy. Although f changes from 0.3 to 1 Hz, each large current peak is relatively stable and bigger than 10 μA. Here this result intuitively shows the superior characteristic of SR-TENG which can effectively convert extremely low-frequency mechanical energy into a relatively stable and controllable electrical output.

In order to analyze the influence of external excitations on the intermittent rotation mode of SR-TENG, the peak current, the maximum current output frequency ($f_{I_{max}}$), and the energy storage time of SR-TENG under different values of A and f were measured. $f_{I_{max}}$ is defined as shown in Figure S8, Supporting Information ($f_{I_{max}} = \dfrac{1}{\dfrac{(t_2 - t_1)}{2}}$). As shown in Figure 4b,c, the peak
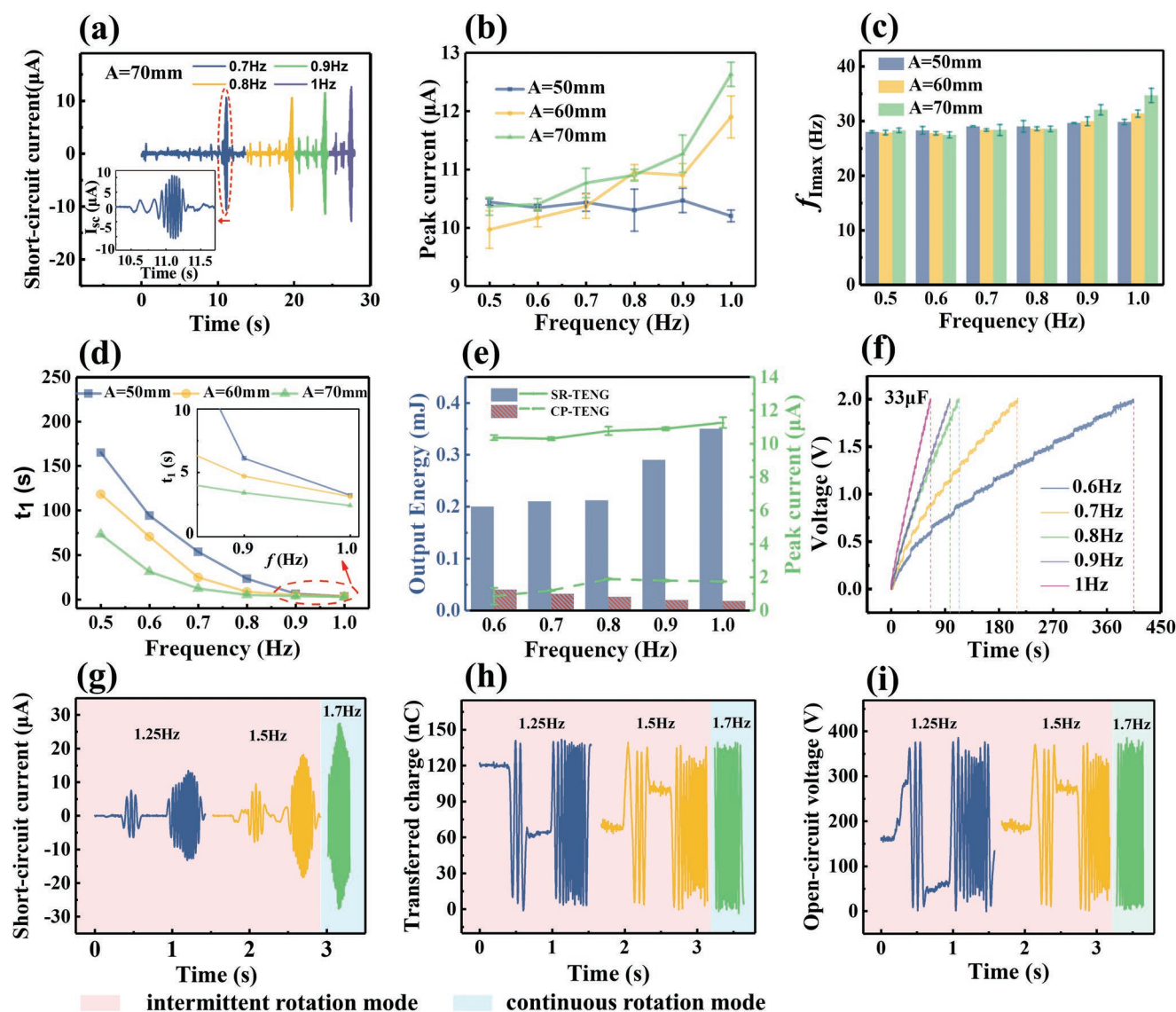
Figure 4. The output performance of SR-TENG under intermittent rotation mode. a) The short-circuit current of SR-TENG at different frequencies under the condition A = 70 mm. The dependence of b) peak current, c) maximum current output frequency, and d) energy storage time on the frequency with various amplitudes. e) Comparison of output energy over one period and peak current of SR-TENG and CP-TENG at different frequencies under A = 70 mm. f) Charging performance of the SR-TENG under A = 70 mm. g) The short-circuit current, h) transferred charge, and i) open-circuit voltage with the frequency ranging from 1.25 to 1.7 Hz under A = 70 mm.

current and the f_{Imax} are almost unchanged in the frequency band of 0.5–0.8 Hz and the amplitude range of 50–70 mm. The peak current is between 10 and 11 μA and the f_{Imax} is about 28 Hz, which proves the broadband and output-controllable property of the SR-TENG. We also study the f_{Imax} of CP-TENG with the same interdigital electrodes shown in Figure S9, Supporting Information. The up-frequency effect of CP-TENG is greatly affected by the excitation frequency. The lower excitation frequency, the lower value of f_{Imax}. By contrast, the up-frequency trend of SR-TENG at extremely low frequency is relatively more stable and higher than CP-TENG. When f reaches 0.9 Hz, the energy release stage is the coupling release of gravitational potential energy and initial rotational kinetic energy, so the peak current and f_{Imax} increase. As demonstrated in Figure 4d,

at the same frequency, the higher excitation amplitude, the smaller value of t_1. The reason is that the higher amplitude can make SR-TENG obtain higher energy. But the interesting thing is that the value of t_1 required for the three amplitudes gradually approaches as f increases, and the value of t_1 is about 3 s under f = 1 Hz. This means that increasing f can make up for the disadvantage that requiring longer energy storage time at a lower amplitude.

In order to prove that the SR-TENG has better performance than traditional CP-TENG (The production process of CP-TENG can be seen in the Experimental Section), we continue to do comparative experiments. In the experiment, the excitation amplitude is fixed as 70 mm. Figure 4e presents the comparison about the output energy in one period and the peak

ADVANCED
SCIENCE NEWS

www.advancedsciencenews.com

ADVANCED
ENERGY
MATERIALS

www.advenergymat.de

current of SR-TENG and CP-TENG. The calculation formula of the output energy of TENG is as follows:

$$E_{out} = \int_0^T I(t)^2 R dt \tag{8}$$

where T is the operational period of TENG, I(t) is the current across the resistor at the time t, and R is the resistance.

On one hand, SR-TENG accumulates 0.2 mJ electric energy in one period of 32 s under $f = 0.6$ Hz, and accumulates 0.35 mJ electric energy in one period of 2 s when $f = 1$ Hz. This also shows the ability of SR-TENG to collect energy efficiently under extremely low frequency. On the other hand, it is far away from the resonance frequency of CP-TENG (≈ 1.8 Hz), so CP-TENG hardly works, the output energy and peak current are very small. At the same frequency and the same statistics time, SR-TENG has significant advantages in both peak current and output energy when $f = 0.5$–1 Hz. Figure 4f demonstrates its power supply capability by charging a 33 µF capacitor. The 33 µF capacitor can be charged to 2 V in 405 s under $f = 0.6$ Hz. As f increases, the time required is significantly reduced. It only takes about 67 s to charge the capacitor to 2 V when $f = 1$ Hz.

Figure 4g–i demonstrates the measured results of I_{sc}, transferred charge (Q_{sc}) and open-circuit voltage (V_{oc}) of the SR-TENG under different excitation frequencies and fixed A = 70 mm. SR-TENG has I_{sc} value of 13.4 µA under $f = 1.25$ Hz. As f increases, SR-TENG automatically switches to continuous rotation mode under $f = 1.7$ Hz, and the value of I_{sc} (Figure 4g) increases significantly to 27.7 µA. The value of Q_{sc} (Figure 4h) and V_{oc} (Figure 4i) remain unchanged ($Q_{sc} = 150$ nC, $V_{oc} = 385$ V). It should be noted here that threshold frequency decreases slightly when A = 70 mm. If f is too high, the swinging component presents a chaotic state.

2.4. Output Performance of SR-TENG under Continuous Rotation Mode

The electrical output performance of SR-TENG under continuous rotation mode is studied in this part. **Figure 5**a and Figure S10, Supporting Information, illustrate the measured results of I_{sc} and Q_{sc} of the SR-TENG versus different excitation amplitudes with fixed $f = 2$ Hz. The curves show that continuous rotation mode can be realized when A is changed from 20 to 30 mm. The peak value of I_{sc} increases from 20.7 to 23.2 µA with increasing A, but the value of Q_{sc} remains almost unchanged and is about 150 nC. Then we studied the effect of excitation frequency on the output performance of SR-TENG in the continuous amplitude range. As shown in Figure 5b, the peak value of I_{sc} shows a monotonic variation from 21.4 to 37.2 µA when f increases from 1.8 to 5 Hz. As shown in Figure S11, Supporting Information, when f increases from 1.8 to 5 Hz, the period decreases from 0.47 to 0.2 s, and the output frequency has a good linear relationship with the excitation frequency, this shows that the output regularity of continuous rotation mode is also controllable. This means that under irregular external excitation conditions, SR-TENG can work with controllable output regularity in continuous rotation mode. Figure 5c illustrate comparison results of the peak current of SR-TENG and CP-TENG versus different

f with A = 20 mm. Owing to the superior coupling method, the output performance of SR-TENG increases significantly with increasing f, while CP-TENG only has high output near the resonance frequency, and the electrical output drops sharply away from resonance frequency. Figure S12, Supporting Information, further illustrates the peak current of the TENG versus different f with a = 3 m s⁻². The curve shows that SR-TENG has an effective working frequency band of about 2.25 Hz, but the effective working frequency bandwidth of CP-TENG is only about 0.5 Hz. Figure S13, Supporting Information, illustrates that SR-TENG has an effective working frequency bandwidth greater than 2.25 Hz under various small accelerations, too.

As demonstrated in Figure 5d, with increasing f, the output energy increases significantly from 0.98 to 1.82 mJ in one period. We calculated the mechanical-electrical conversion efficiency(η) of SR-TENG at various frequencies by using the following equation:

$$\eta = \frac{E_{out}}{E_{in}} = \frac{\int_0^T I(t)^2 R dt}{2m_{II}gl_{II} + \int_0^\pi M_R d\theta} \tag{9}$$

where M_R and θ are the resistance torque and the angular displacement of rotor, respectively. The value of M_R of SR-TENG measured by the torque sensor is about 25 mN m. So the calculated value of η increase from 11.5% to 21.9% with increasing f from 1.8 to 5 Hz, as shown in Figure 5d.

The performance of the SR-TENG for harvesting low-frequency mechanical energy with multiple directions is studied here, and the schematic diagram of the experimental setup is shown in Figure S14a, Supporting Information. The angle between the vertical direction of the linear motor's motion direction and the central axis of the SR-TENG is defined as θ. As can be observed in Figure S14b,c, Supporting Information, I_{sc} gradually decreases with θ. When θ is changed from 0° to 45°, SR-TENG works in continuous rotation mode. When $\theta = 60°$, SR-TENG enters intermittent rotation mode. It is worth mentioning that SR-TENG can still realize energy harvesting even when $\theta = 75°$, unlike CP-TENG. [10] Figure 5e and Figure S14d, Supporting Information, illustrate the peak value of I_{sc} and Q_{sc} of the SR-TENG versus different θ for various excitation frequencies. SR-TENG exhibits good multidirectional energy harvesting capability in a wide frequency band. Compared with general TENGs,[15] the output performance of SR-TENG to harvest energy with multiple directions is obviously better.

Then the charging capability of SR-TENG was also investigated, as presented in Figure 5f. For the capacitors of 100 µF, when f increases from 1.8 to 5 Hz, the time required for the capacitor to be charged to 11 V has been reduced from 177 to 70 s. Figure 5g shows the peak value of I_{sc}, peak power (P_p), and average power (P_a) versus different load resistance (R) under the excitation ($f = 1.8$ Hz and A = 20 mm). The peak power and the average power are calculated by the formula:

$$P_p = I_{max}^2 R \tag{10}$$
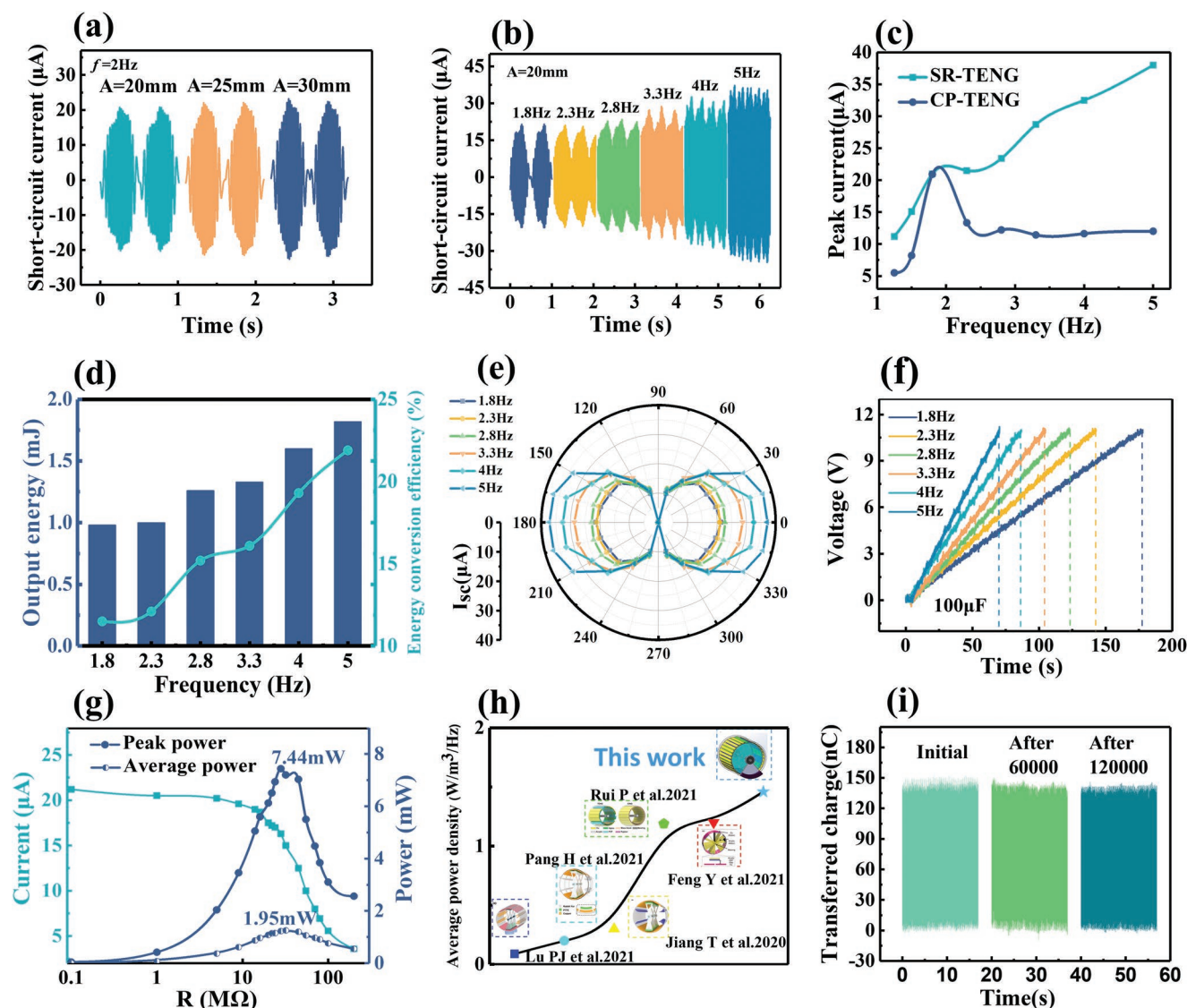
$$P_a = \frac{\int_0^T I^2 R dt}{T} \tag{11}$$

Figure 5. The output performance of SR-TENG under continuous rotation mode. a) The short-circuit current with the amplitude ranging from 20 to 30 mm under the condition $f = 2$ Hz. b) The dependence of short-circuit current on the frequency under $A = 20$ mm and c) comparison of peak current of SR-TENG and CP-TENG at different frequencies under $A = 20$ mm. d) The dependence of output energy and energy conversion efficiency in one period on the frequency under $A = 20$ mm. e) The dependence of short-circuit current with the angle ranging from 0° to 360° on the frequency under $A = 20$ mm. f) Charging performance of the SR-TENG under $A = 20$ mm. g) Dependence of the output current, peak power and average power for SR-TENG on the resistance of the load at 1.8 Hz. h) Comparison of average power density between SR-TENG and CP-TENG. Reproduced with permission.[16a] Copyright 2020, Wiley-VCH. Reproduced with permission.[16b] Copyright 2021, Wiley-VCH. Reproduced with permission.[9b] Copyright 2021, Elsevier. Reproduced with permission.[9c] Copyright 2021, Wiley-VCH. Reproduced with permission.[9d] Copyright 2021, American Chemical Society. i) Electrical output durability of SR-TENG after 120 000 cycles of continuous testing.

where I_{max} is the peak value of the instantaneous current. The calculation result in Figure 5g indicates that the value of P_p and P_a reach the maximum of 7.44 mW (power density of 10.1 W m^{-3}) and 1.95 mW (power density of 2.64 W m^{-3}) when the load resistance is around 28 MΩ. Figure 5h compares the average power density of the SR-TENG ($f = 1.8$ Hz) with the previous contactless CP-TENG.[9b–d,16] This shows that SR-TENG can achieve higher energy harvesting performance. The resistance dependence of the output performance for the SR-TENG under $f = 5$ Hz was also characterized, as shown in Figure S15a, Supporting Information. The value of P_p and P_a reach the maximum of 11.33 mW (power density of 15.4 W m^{-3}) and 3.6 mW (power density of 4.9 W m^{-3}) when the load resistance is around

20 MΩ. Figure S15b, Supporting Information, demonstrates the SR-TENG's ability to charge larger capacitors when $f = 5$ Hz, the charged voltage for the capacitors of 220, 330, 470, and 1000 µF can reach 5.5, 3.4, 2.6, and 1.3 V in 60 s, respectively. As shown in Figure 5i, after 120 000 cycles of continuous testing (700 min), the SR-TENG still maintains 96% electrical output under the triggering conditions of $i = 5:1$, $A = 20$ mm and $f = 3$ Hz. Figure S16, Supporting Information, exhibits the optical microscope images of the surface of materials on the rotor. It can be seen that there is only slight wear on the surface of Nylon and FEP film after continuous testing of 120 000 cycles. This superior durability is attributed to the flexible charge-pump design and non-contact properties of SR-TENG.

2.5. Demonstration of Harvesting Low-Frequency Mechanical Energy

First, SR-TENG can be used to harvest low-frequency mechanical energy to power small electronic devices. As shown in Figure S17a, Supporting Information, the output voltage of SR-TENG was regulated by a rectifier, a 220 µF capacitor is charged and then is used to power some devices under the motor trigger condition $f = 1.8$ Hz, $i = 5:1$, and $A = 20$ mm. As shown in **Figure 6**a, the SR-TENG can drive a temperature/humidity meter after the voltage of the capacitor was charged from 0 to 1.86 V in 46 s. Moreover, the meter can continuously measure the temperature and humidity of the external environment for 14 s, and then the meter can display the measured parameters every 4s. The demonstration of this experiment

is given in Video S2, Supporting Information. Then, the SR-TENG was used to continuously power a calculator and an electronic watch, as demonstrated in Figure 6b and Figure S17b and Videos S3 and S4, Supporting Information. Meanwhile, the SR-TENG successfully powered 1020 LEDs (Figure S17c, Supporting Information) at 1.8 Hz and 1620 LEDs (Figure 6c) at 5 Hz, as shown in Videos S5 and S6, Supporting Information.

As shown in Figure 6d, this diagram shows that low-frequency water wave energy in the marine environment can be harvested by SR-TENG, and the power management module was integrated with the TENG to supply power to the terminal unit, which is helpful for building smart ocean. This is a complete self-powered and closed-loop system. The SR-TENG could be made into an ocean buoy to harvest ocean energy. To demonstrate the output performance of SR-TENG for harvesting water
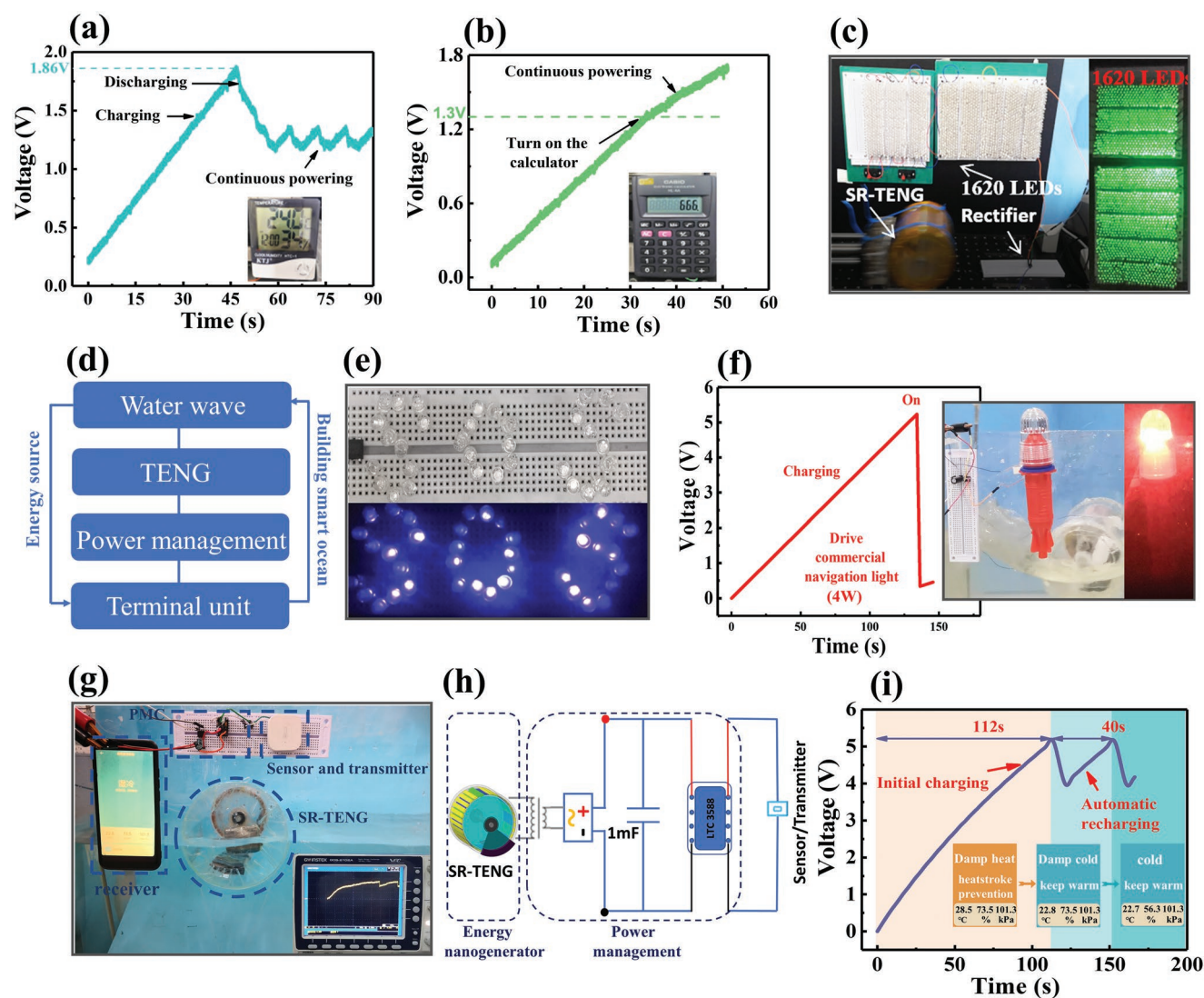

Figure 6. The demonstration of the SR-TENG harvesting low-frequency mechanical energy and driving low-power electronic devices. The voltage curve for the SR-TENG to power a) a temperature/humidity meter and b) a calculator under $f = 1.8$ Hz. c) The photographs for powering 1620 LEDs by linear motor under $f = 5$ Hz. d) The diagram of a self-powered and closed-loop system and e) the photographs for powering SOS-style UV lights by water wave. f) The voltage curve for powering commercial navigation light by water wave. g) Actual image of a temperature/humidity monitoring and wireless signal transmission system. h) Circuit diagram of the temperature/humidity monitoring and wireless signal transmission system. i) The capacitor's voltage versus time when the temperature/humidity monitoring and wireless signal transmission system is working.

**ADVANCED
SCIENCE NEWS**

www.advancedsciencenews.com

**ADVANCED
ENERGY
MATERIALS**

www.advenergymat.de

wave energy, the experimental setup is tied to the bottom wall of the water tank by ropes, and the water wave is generated by a motor-driven push plate. Figure 6e and Video S7, Supporting Information. show that SR-TENG successfully powers the SOS-style UV lights, which can be used for marine rescue, and the UV lights also can expel marine microorganisms and prevent them from adhering to the sensor. In addition, as shown in Video S8, Supporting Information, a 470 µF capacitor was used for electrical energy storage. When it was charged to 5 V, the switch was turned on to drive the commercial navigation light (4 W). The voltage curve on the capacitor for the charging and discharging process is shown in Figure 6f. Finally, a self-powered temperature/humidity monitoring and wireless signal transmission system based on the SR-TENG is demonstrated in Figure 6g. Figure 6h shows the corresponding circuit diagram. The output energy of SR-TENG first passes through a transformer and a rectifier bridge, and then the electric energy is stored in a 1 mF capacitor. Subsequently, a commercial energy harvester microchip LTC3588 is used to further stabilizes the electric energy and generate a stable voltage to drive the temperature/humidity sensor and transmitter. In the experiment, the mobile phone and the transmitter are connected through the Wi-Fi network, so the remote transmission of meteorological signal can be realized. The voltage on the 1 mF capacitor is captured by an oscilloscope in time and the voltage versus time is shown in Figure 6i. After initial charging a 1 mF capacitor for 112 s, the power management circuit can generate a voltage of 5.2 V to drive the sensor and transmitter to work for the first time. Then the phone can receive a temperature/air pressure/humidity signal from the system every 40 s. The corresponding visual demonstration can be found in Video S9, Supporting Information. These applications show that SR-TENG can harvest low-frequency mechanical energy to meet energy supply requirements. This experiment demonstrates the potential of the SR-TENG fabricated into buoys to harvest water wave energy as sustainable electricity.

3. Conclusion

In summary, a triboelectric nanogenerator enabled by coupling swing-rotation switching mechanism with potential energy storage/release strategy for efficiently harvesting low-frequency mechanical energy is proposed in this work. The swing-rotation switching mechanism can convert various vibration/swing motion with wide bandwidth into rotary motion. Meanwhile, the rotary mechanical energy can be stored as the gravitational potential energy first and then is released totally for one time and periodically. The potential energy storage/release strategy makes SR-TENG switch automatically between the intermittent and continuous rotation mode. When SR-TENG works in the intermittent rotation mode, it converts the extremely low-frequency mechanical energy (≤ 1 Hz) into steady electric energy. In the continuous rotation mode, the output performance and mechanical-electrical conversion efficiency of SR-TENG increase significantly with the excitation frequency. The peak power density and average power density of SR-TENG reach 10.1 and 2.64 W m^{-3} at 1.8 Hz, 15.4 and 4.9 W m^{-3} at 5 Hz, respectively. Compared with the traditional cylindrical pendulum triboelectric nanogenerators (CP-TENG) that just efficiently operate around their resonant frequency, SR-TENG exhibits superior performance in low-frequency energy harvesting. After that, SR-TENG was demonstrated to successfully drive several small electronic devices and light up 1620 LEDs. Finally, in a water tank, successful demonstrations on night direction indication, marine lighting and rescue, the expulsion of microorganisms, ambient temperature/humidity detection are presented. They show the potential applications of the SR-TENG in the smart ocean in future.

4. Experimental Section

Fabrication of the SR-TENG and CP-TENG: The SR-TENG mainly consisted of internal rotor, external stator, and the swing-rotation switching structure. The stator and rotor were both made of acrylic cylinder. The inner wall of the acrylic stator (diameter: 100 mm; height: 90 mm) adhered with 28 Cu electrodes (width: 8.5 mm; length: 85 mm; thickness: 65 µm) and two-blade FEP films (width: 15 mm; length: 90 mm; thickness: 30 µm). On the outer wall of the acrylic rotor (diameter: 90 mm; height: 75 mm), 16 equally spaced and parallel Nylon films (width: 8.5 mm; length: 75 mm; thickness: 25 µm) were uniformly attached to the FEP film (width: 8.5 mm; length: 75 mm; thickness: 30 µm). The inner wall of the rotor adhered with the mass block II, and there was a gap (about 1.3 mm) between the rotor and the stator. The swing-rotation switching structure mainly included an acrylic central shaft (length: 150 mm; axle diameter: 8 mm), an acrylic arc swinging component (60°), two one-way clutches (outer diameter: 22 mm; inner diameter: 8 mm), one two-way clutch (outer diameter: 16 mm; inner diameter: 8 mm), and there was mass block II on the outer swinging part, in addition, replacing the two one-way clutches of SR-TENG device with two bearings, which was the CP-TENG device in the experimental test.

Electrical Measurement: The output electrical performance of the SR-TENG was measured by the electrometer (6514, Keithley, USA). The data acquisition and analysis platform consisted of a data acquisition card (NI, USB 6211) and LabVIEW. SR-TENG was driven by a commercial motor (ZD-5IK40W, China). A non-contact magnetic induction angle sensor was used to monitor the change of rotation angle (P3022, 0–360°, 0–5 V, China). A microcircuit chip (LTC3588, LINEAR, Shanghai, China) was used as part of the circuit management module. The temperature/air pressure/humidity sensor (BMP180, XIAOMI, Beijing, China) was used to measure external environmental parameters. A dual-channel oscilloscope (GDS-2102A, GUWEI, Taiwan, China) was used to measure the voltage in the experimental demo.

Supporting Information

Supporting Information is available from the Wiley Online Library or from the author.

Conflict of Interest

The authors declare no conflict of interest.

Data Availability Statement

The data that support the findings of this study are available from the corresponding author upon reasonable request.

[1] A. Shahsavari, M. Akbari, *Renewable Sustainable Energy Rev.* **2018**, *90*, 275.

[2] a) F. Monforti, T. Huld, K. Bodis, L. Vitali, M. D'Isidoro, R. Lacal-Arantegui, *Renewable Energy* **2014**, *63*, 576; b) S. Kosunalp, I. Access, **2016**, *4*, 5755.

[3] Z. L. Wang, *Nano Energy* **2019**, *58*, 669.

[4] a) S. Wang, Z. Lin, S. Niu, L. Lin, Y. Xie, K. C. Pradel, Z. L. Wang, *ACS Nano* **2013**, *7*, 11263; b) D. Larcher, J. M. Tarascon, *Nature Chem.* **2015**, *7*, 19.

[5] a) X. Liang, T. Jiang, G. Liu, Y. Feng, C. Zhang, Z. L. Wang, *Energy Environ. Sci.* **2020**, *13*, 277; b) C. Wu, A. C. Wang, W. Ding, H. Guo, Z. L. Wang, *Adv. Energy Mater.* **2019**, *9*, 1802906; c) S. Fu, W. He, Q. Tang, Z. Wang, W. Liu, Q. Li, C. Shan, L. Long, C. Hu, H. Liu, *Adv. Mater.* **2022**, *34*, 2105882; d) Y. Zhong, H. Zhao, Y. Guo, P. Rui, S. Shi, W. Zhang, Y. Liao, P. Wang, *Adv. Mater. Technol.* **2019**, *4*, 1900741; e) C. Zhang, W. Tang, C. Han, F. Fan, Z. L. Wang, *Adv. Mater.* **2014**, *26*, 3580; f) Y. Zi, H. Guo, Z. Wen, M. H. Yeh, C. Hu, Z. L. Wang, *ACS Nano* **2016**, *10*, 4797.

[6] a) C. Zhang, L. He, L. Zhou, O. Yang, W. Yuan, X. Wei, Y. Liu, L. Lu, J. Wang, Z. L. Wang, *Joule* **2021**, *5*, 1613; b) W. Liu, L. Xu, T. Bu, H. Yang, G. Liu, W. Li, Y. Pang, C. Hu, C. Zhang, T. Cheng, *Nano Energy* **2019**, *58*, 499; c) T. Xiao, X. Liang, T. Jiang, L. Xu, J. Shao, J. Nie, Y. Bai, W. Zhong, Z. L. Wang, *Adv. Funct. Mater.* **2018**, *28*, 1900741.

[7] a) F. Xi, Y. Pang, G. Liu, S. Wang, W. Li, C. Zhang, Z. L. Wang, *Nano Energy* **2019**, *61*, 1; b) P. Wang, R. Liu, W. Ding, P. Zhang, L. Pan, G. Dai, H. Zou, K. Dong, C. Xu, Z. L. Wang, *Adv. Funct. Mater.* **2018**, *28*, 1705808; c) X. Lu, H. Zhang, H. Zhao, H. Yang, L. Zheng, W. Wang, C. Sun, *Nano Energy* **2021**, *89*, 106352; d) C. Zhang, L. Zhou, P. Cheng, D. Liu, C. Zhang, X. Li, S. Li, J. Wang, Z. L. Wang, *Adv. Energy Mater.* **2021**, *11*, 2003616; e) G. Zhu, J. Chen, T. Zhang, Q. Jing, Z. L. Wang, *Nat. Commun.* **2014**, *5*, 3426.

[8] a) L. Pan, J. Wang, P. Wang, R. Gao, Y. Wang, X. Zhang, J. Zou, Z. L. Wang, *Nano Res.* **2018**, *11*, 4062; b) X. Hang, T. Jiang, G. Liu, T. Xiao, L. Xu, W. Li, F. Xi, C. Zhang, Z. L. Wang, *Adv. Funct. Mater.* **2019**, *29*, 1807241; c) M. Xu, P. Wang, Y. Wang, S. L. Zhang, A. C. Wang, C. Zhang, Z. Wang, X. Pan, Z. L. Wang, *Adv. Energy Mater.* **2018**, *8*, 1702432; d) Z. L. Wang, M. Today, **2017**, *20*, 74;

[9] a) Y. Feng, T. Jiang, X. Liang, J. An, Z. L. Wang, *Appl. Phys. Rev.* **2020**, *7*, 021401; b) Y. Feng, X. Liang, J. An, T. Jiang, Z. L. Wang, *Nano Energy* **2021**, *81*, 105625; c) P. Lu, H. Pang, J. Ren, Y. Feng, J. An, X. Liang, T. Jiang, Z. L. Wang, *Adv. Mater. Technol.* **2021**, *6*, 2100496; d) P. Rui, W. Zhang, P. Wang, *ACS Nano* **2021**, *15*, 6949.

[10] P. Rui, W. Zhang, Y. Zhong, X. Wei, Y. Guo, S. Shi, Y. Liao, J. Cheng, P. Wang, *Nano Energy* **2020**, *74*, 104937.

[11] a) R. Ding, Z. Cao, Z. Wu, H. Xing, X. Ye, *ACS Nano* **2021**, *15*, 16861; b) P. Wang, L. Pan, J. Wang, M. Xu, G. Dai, H. Zou, K. Dong, Z. L. Wang, *ACS Nano* **2018**, *12*, 9433; c) Y. Wang, X. Yu, M. Yin, J. Wang, Q. Gao, Y. Yu, T. Cheng, Z. L. Wang, *Nano Energy* **2021**, *82*, 105740; d) J. Yu, X. Wei, Y. Guo, Z. Zhang, P. Rui, Y. Zhao, W. Zhang, S. Shi, P. Wang, *Lab Chip* **2021**, *21*, 284.

[12] M.-L. Seol, J.-W. Han, D.-I. Moon, K. J. Yoon, C. S. Hwang, M. Meyyappan, *Nano Energy* **2018**, *44*, 82.

[13] M. Yin, X. Lu, G. Qiao, Y. Xu, Y. Wang, T. Cheng, Z. L. Wang, *Adv. Energy Mater.* **2020**, *10*, 2000627.

[14] H. Guo, J. Chen, M.-H. Yeh, X. Fan, Z. Wen, Z. Li, C. Hu, Z. L. Wang, *ACS Nano* **2015**, *9*, 5577.

[15] a) Z. Lin, B. Zhang, H. Guo, Z. Wu, H. Zou, J. Yang, Z. L. Wang, *Nano Energy* **2019**, *64*, 103908; b) M. Xu, T. Zhao, C. Wang, S. L. Zhang, Z. Li, X. Pan, Z. L. Wang, *ACS Nano* **2019**, *13*, 1932.

[16] a) T. Jiang, H. Pang, J. An, P. Lu, Y. Feng, X. Liang, W. Zhong, Z. L. Wang, *Adv. Energy Mater.* **2020**, *10*, 2000064; b) H. Pang, Y. Feng, J. An, P. Chen, J. Han, T. Jiang, Z. L. Wang, *Adv. Funct. Mater.* **2021**, *31*, 2106398;